Multi-angle aerosol optical depth retrieval method based on improved surface reflectance

Lijuan Chen[1], Ren Wang[1], Ying Fei[2], Peng Fang[2],Yong Zha[2], Haishan Chen[1*]

[1]Key Laboratory of Meteorological Disaster, Ministry of Education (KLME)/Joint International

Research Laboratory of Climate and Environment Change (ILCEC)/Collaborative Innovation

Center on Forecast and Evaluation of Meteorological Disasters (CIC-FEMD), Nanjing University

of Information Science and Technology, Nanjing 210044, China

[2]Key Laboratory of Virtual Geographic Environment of Ministry of Education, Jiangsu Center for

Collaborative Innovation in Geographical Information Resource Development and Application,

College of Geographic Science, Nanjing Normal University, Nanjing 210023, China

Correspondence: Haishan Chen (haishan@nuist.edu.cn)

Abstract

Retrieval of atmospheric aerosol optical depth (AOD) has been a challenge for Earth satellite observations, mainly due to the difficulty in estimating surface reflectance with the combined influence of land-atmosphere coupling. Current major satellite AOD retrieval products have low spatial resolution under complex surface processes. In this study, we further improved the surface reflectance by modeling the error correction based on the previous AOD retrieval and obtained more accurate AOD retrieval results. A lookup table was constructed using the Second Simulation of Satellite Signal in the Solar Spectrum (6S) to enable high-precision AOD retrieval. The accuracy of the algorithm's retrieval was verified by the Aerosol Robotic Network observations (AERONET). From the validation results, we find that among the nine Multi-angle Imaging

22   SpectroRadiometer (MISR) angles, the retrieved AOD has the best retrieved results with the AOD

23   observed at the An angle (Taihu: R=0.81, RMB=0.68; Xuzhou-CUMT: R=0.73, RMB=0.78). This

24   study will help to further improve the retrieval accuracy of multi-angle AOD at large spatial scales

25   and long time series. The retrieved AOD based on the improved method has the advantages of

26   fewer missing pixels and finer spatial resolution compared to the MODIS AOD products and our

27   previous estimates.

28   Keywords: surface reflectance; aerosol optical depth; satellite remote sensing; MISR; MODIS

29   **1. Introduction**

30   Aerosols are liquid or solid particles suspended in the atmosphere, with particle diameters

31   ranging from approximately 0.001 to 100 μm (Giles et al., 2019). Aerosol particles suspended in

32   the atmosphere not only affect the radiative forcing of the Earth's air system through direct,

33   indirect or semi-direct action, but also influence climate, and cause environmental problems such

34   as acid rain and haze (Hatzianastassiou et al., 2009; Dao et al., 2014; Daniel et al., 2014; Samset et

35   al., 2018; Li et al., 2018; Huang et al., 2021). Therefore, the study of aerosol distribution and

36   change trend has become a hot topic in the field of aerosol research (Holben et al., 2001; Li et al.,

37   2020; Berhane et al., 2021; Sun et al., 2022). In addition, high concentrations of aerosols can pose

38   a serious threat to human health (Lee et al., 2010; Dehghani et al., 2012; Mironova et al., 2015).

39   The optical properties of aerosols include parameters such as aerosol optical depth (AOD),

40   scattering phase function, single scattering albedo, and absorbing optical depth. Among them,

41   AOD is an important parameter defined as the integral of the aerosol extinction coefficient in the

42   vertical direction. It describes the attenuation effect of aerosols on light and is an important

43   indicator of the level of air pollution. Multi-channel spectrometers on board geostationary and

polar orbiting satellites have been used for AOD retrieval in the last two decades. The AOD

products obtained through satellite retrievals are widely used in atmospheric environmental

studies (Kaufman et al, 1997; Xie et al., 2019; Chen et al., 2021). Although the accuracy of AOD

retrieval has been improving, there is still much room for improvement in the AOD retrieval on

land when more complex influences are taken into account.

Scholars have conducted research on AOD retrieval using satellite-based multi-angle sensors.

Kokhanovsky et al. (2009) used the Along-Track Scanning Radiometer Dual View (ATSR-DV)

algorithm to retrieve AOD over Germany and compared the retrieval results with the Medium

Resolution Imaging Spectrometer (MERIS) and Multi-angle Imaging SpectroRadiometer (MISR)

products. The results show that the ATSR-2 algorithm is also applicable to the Advanced

Along-Track Scanning Radiometer (AATSR). Sundstrom et al. (2012) obtained an aerosol model

of eastern China based on Aerosol Robotic Network (AERONET) observation data and used the

ATSR-DV algorithm to retrieve the proportion of AOD and coarse to fine particles from AATSR

data. Abdou et al. (2005) compared the MISR AOD and the Moderate-resolution Imaging

Spectroradiometer (MODIS) AOD products carried by Terra using data from 62 AERONET

observation sites. The results show that over land, the MODIS AOD of 0.470 um and 0.660 um

channels is 35% and 10% higher than that of MISR, respectively. In coastal and desert areas,

MODIS retrieval error is large, while over the ocean, at 0.470 um and 0.660 um channels, MISR is

0.1 and 0.05 higher than MODIS AOD value, mainly depending on the accuracy of radiometric

calibration. Martochik et al. (1997) proposed an algorithm for extracting aerosol optical

parameters using MISR multi-angle observations. The results show that the low reflectance of

vegetation and multi-angle observation data are used to retrieve AOD in the case of dense land

66   vegetation. As a new remote sensing tool, multi-angle remote sensing can provide aerosol optical

67   depth, single scattering albedo, phase function and other features with sufficient accuracy, which

68   is more suitable for playing its unique role in aerosol research than traditional single-angle optical

69   remote sensing (Dubovik et al., 2019). Multi-angle remote sensing retrieval of aerosol optical

70   properties can use the angle information contained in satellite signals to better separate the

71   contributions of the surface and atmosphere, which is suitable for some bright surfaces. This

72   provides a new way for AOD retrieval.

73   Surface reflectance measures the ability of land to absorb and reflect solar radiation. On land,

74   surface reflectance is relatively complex and is detected by satellite sensors after atmospheric

75   scattering and absorption. Satellite observations capture the combination of there two components,

76   making it challenging to directly separate surface reflectance from atmospheric scattering.

77   Therefore, simultaneous acquisition of atmospheric aerosols and surface reflectance is the main

78   objective of quantitative satellite remote sensing (Deuzé et al., 2001). In optical remote sensing,

79   the blue wavelength is shorter and the surface reflectance is lower, resulting in more atmospheric

80   reflection and scatteringm. Blue band is commonly used for AOD retrieval. In the process of AOD

81   retrieval, overestimation of surface reflectance leads to underestimation of AOD, while

82   underestimation of surface reflectance leads to overestimation of AOD. In general, aerosol signals

83   are weaker than surface signals (Dong et al., 2023). Previous studies have shown that when the

84   surface reflectance intercept error is 0.01, the error of satellite remote sensing retrieval AOD is

85   about 0.1 (Zhang et al., 2021). Therefore, accurate estimation of surface reflectance is very

86   importance for the accurate retrieval of aerosol optical depth.

87   In order to improve the accuracy and resolution of MISR AOD retrieval, we analyzed the

88 MISR AOD retrieval errors of 9 camera angles in previous studies. Secondly, by establishing an

89 error correction model, we modify the surface reflectance of MISR to improve the accuracy of

90 surface reflectance estimation. Finally, the improved AOD is verified with the ground observation

91 site AOD data, and the retrieval results are compared with the previous retrieval results and

92 MODIS AOD products.

93 **2. MISR, MODIS, and AERONET Data**

94 **2.1 MISR data**

95   In this study, we employed MISR Level 1B2 terrain data (MI1B2T) and used HEGTool

96 (HDF-EOS To GeoTIFF Conversion Tool) software to extract radiation data. Blocks 64 and 65

97 covering the Yangtze River Delta region were extracted by selecting corresponding blocks, output

98 data types and projections based on the regional locations of 180 blocks (Figure S1). In addition,

99 we extracted the solar zenith angle, solar azimuth angle, satellite zenith angle, and satellite

100 azimuth angle data of 9 cameras from the angle dataset (MI1B2GEOP) and selected the

101 corresponding blocks, output data types and projection information. To reduce the influence of

102 cloud, we carried out cloud detection and cloud pixel removal on satellite remote sensing images

103 with cloud pixel coverage less than 50%, and used blue band threshold to remove cloud pixels.

104 However, through repeated experiments, we found that the fixed threshold was not effective in

105 removing cloud pixels at 9 angles of the MISR sensor (Figures S2 and S3). Therefore, we use

106 dynamic threshold method to remove cloud pixels from MISR data. Details of the data used in this

107 study are shown in Table S2.

2.2 MODIS data

In this study, we used MODIS L1B data, including radiance data (MOD02/MYD02) and geolocation data (MOD03/MYD03). Data preprocessing using the MODIS Conversion Toolkit (MCTK) tool, including radiation calibration, butterfly processing, geometric correction, reprojection, and band extraction. MODIS BRDF/Albedo is a standard Level 3 product that represents the surface characteristics of MODIS instruments on the Terra and Aqua satellite platforms. The product retrieval cycle is 16 days, and the observations on day 9 of each 16-day cycle are weighted to generate daily data, called the global daily surface albedo product (Hsu et al., 2004). The core data set for the MODIS BRDF product is MCD43A1.

2.3 AERONET data

AERONET uses the CE-318 instrument, a solar radiation photometer produced in France, which obtains direct solar spectral radiation measurements at 340, 380, 440, 500, 670, 870, 936, 1020 and 1640 nm channels at 1.5° field angles every 3 min. The total water vapor content of the atmosphere can be obtained in the 936 nm channel. The AOD value can be retrieved by the measured value of other channels, and the retrieval error is about 0.01-0.02. Therefore, it can provide aerosol characteristic parameters with high accuracy and verify aerosol parameters retrieved by satellite (Lu et al., 2019). In this study, AERONET AOD values are used as truth values to verify the accuracy of satellite remote sensing AOD retrieval. AERONET AOD data is classified into three levels: Level 1.0 (unfiltered), level 1.5 (cloud screening and quality control) and level 2.0 (quality assurance). The study area mainly covers the Yangtze River Delta, and there are several ground observation sites in the area. However, only two observation sites, Taihu and

129   Xuzhou-CUMT sites have continuous observation data, while the duration of other sites is

130   relatively limited. Therefore, AERONET Level 1.5 AOD data with a large number of observed

131   values were selected to verify the retrieval results of MISR AOD.

132   **3. Methodology**

133   **3.1 Problems in the previous surface reflectance estimation method**

134   Accurate estimation of surface reflectance is a crucial and challenging aspect in the retrieval

135   of AOD from satellite remote sensing data (Remer et al., 2009; Gupta et al., 2016). Previous

136   research has identified the variation patterns of 9-angle MISR AOD (Chen et al., 2021). However,

137   the AOD retrieved from 9 angles shows relatively large errors compared to AERONET AOD

138   (Table S3). Atmospheric correction can eliminate the effects of clouds and aerosols and obtain true

139   surface reflectance. The reflectance of MISR is calculated by inputting geometric parameters,

140   AOD, aerosol type, sensor radiation brightness data and sensor height into 6S model. In this study,

141   we input MISR geometric parameters and radiation data corresponding to Taihu and

142   Xuzhou-CUMT sites, and AOD parameters are AERONET AOD values of these two sites. The

143   reflectance of atmospheric correction for each pixel is calculated by the linear atmospheric

144   correction formula. To explore the reasons for the high AOD value of the retrieval from 9 MISR

145   angles, the MISR atmospheric correction reflectance and MISR surface reflectance were

146   compared at the corresponding locations of the two sites (Figure 1) (MISR surface reflectance

147   calculation method referenced Chen et al. (2021)). The results show that the surface reflectance of

148   MISR is lower than the atmospheric reflectance of MISR. The MISR AOD retrieved is higher

149   compared to the AERONET AOD. Therefore, it is necessary to establish a correction model to

150 improve the MISR surface reflectance and improve the retrieval accuracy of MISR AOD.
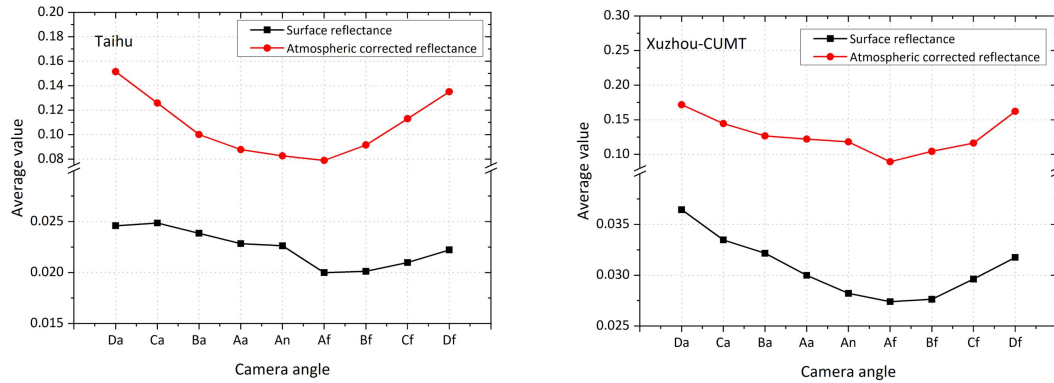
151   **Figure 1.** Comparison of MISR surface reflectance and atmospheric corrected reflectance in blue

152   band (At the pixel locations of Taihu and Xuzhou-CUMT sites).

153   **3.2 Improved surface reflectance estimation method**

154   To construct an improved surface reflectivity correction model, the specific steps are shown

155   as follows:

156   (1) Calculation of MODIS atmospheric corrected reflectance

157   The MODIS L1B data is corrected by the 6S model, and the MODIS atmospheric correction

158   reflectance is obtained. When using 6S model to calculate MODIS atmospheric correction

159   reflectivity, it is necessary to provide geometric parameters, AOD, atmospheric mode, aerosol type,

160   sensor radiance data, sensor height, spectral parameters and other parameters. In this study,

161   MODIS geometric parameters and radiance data corresponding to Taihu and Xuzhou-CUMT sites

162   are used. The AOD parameters were obtained from AERONET AOD data at both sites.

163   Atmospheric models select mid-latitude winter and mid-latitude summer to account for seasonal

164   variations in atmospheric transport. The aerosol type selected in this study is continental aerosol.

165   The sensor height is set to the observation height of the satellite. The spectral parameters are

166 defined according to the band of the MODIS sensor. By providing these parameters, we can

167 calculate the atmospheric correction reflectance of the MODIS sensor using the 6S model.

168 (2) Surface bidirectional reflectance Calculation

169 MODIS BRDF/Albedo product MCD43A1 data and Ross-Li model were used to simulate

170 surface bidirectional reflectance under MODIS and MISR observation geometry. The linear kernel

171 driven BRDF model includes three basic parameters: the reflectance of the lowest point view and

172 the weighting coefficient of the two kernel functions. The model can be calculated using formulas

173 1-9.

174
$$BRDF(\theta_s, \theta_v, \phi) = f_{iso}(\Lambda) + f_{vol}(\Lambda)K_{vol}(\theta_s, \theta_v, \phi) + f_{geo}(\Lambda)K_{geo}(\theta_s, \theta_v, \phi) \qquad (1)$$

175
$$K_{vol}(\theta_s, \theta_v, \phi) = \frac{(\pi/2 - \xi)\cos\xi + \sin\xi}{\cos\theta_s + \cos\theta_v} - \frac{\pi}{4} \qquad (2)$$

176
$$K_{geo}(\theta_s, \theta_v, \phi) = O(\theta_s, \theta_v, \phi) - \sec\theta'_s - \sec\theta'_v + \frac{1}{2}(1 + \cos\xi')\sec\theta'_s \sec\theta'_v \qquad (3)$$

177
$$O(\theta_s, \theta_v, \phi) = \frac{1}{\pi}(t - \sin t \cos t)(\sec\theta'_s + \sec\theta'_v) \qquad (4)$$

178
$$\cos t = \frac{h}{b} \frac{\sqrt{D^2 + (\tan\theta'_s \tan\theta'_v \sin\phi)^2}}{\sec\theta'_s + \sec\theta'_v} \qquad (5)$$

179
$$D = \sqrt{\tan^2\theta'_s + \tan^2\theta'_v - 2\tan\theta'_s \tan\theta'_v \cos\phi} \qquad (6)$$

180
$$\cos\xi' = \cos\theta'_s \cos\theta'_v + \sin\theta'_s \sin\theta'_v \cos\phi \qquad (7)$$

181
$$\theta'_s = \tan^{-1}(\frac{b}{r}\tan\theta_s) \qquad (8)$$

182
$$\theta'_v = \tan^{-1}(\frac{b}{r}\tan\theta_v) \qquad (9)$$

183 In the above equations, $BRDF(\theta_s, \theta_v, \phi)$ is the surface bidirectional reflectance, while θ_s,

184 θ_v, and ϕ are the solar zenith angle, the satellite zenith angle, and relative azimuth angle,

185 respectively. Λ is bandwidth, while $K_{vol}(\theta_s, \theta_v, \phi)$ and $K_{geo}(\theta_s, \theta_v, \phi)$ are volumetric scattering

186 kernel and geometric optical scattering kernel, respectively, which are functions of the angle of

187 incidence and the angle of observation. f_{iso}, f_{vol}, and f_{geo} are the weights assigned to

188 isotropic scattering, volumetric scattering, and geometric optical scattering, respectively. ξ is the

189 scattering angle, while b, h, and r represent vertical radius of the sphere, horizontal radius of the

190 sphere and height of the center of the sphere, respectively. These three parameters can be defined

191 as fixed values. In the production process of the MODIS BRDF model, the relationship between h,

192 b and r parameters is h/b=2 and b/r=1 (Schaaf et al., 1999). According to the above equation, the

193 surface bidirectional reflection under any incident direction of the sun and observation direction of

194 the satellite can be obtained by extrapolating the nucleus.

195   (3) Improved MISR surface reflectance calculation

196   The MODIS atmospheric correction reflectance is brought into Eq. 10 and Eq. 11, and a new

197 MISR surface reflectance estimate based on MODIS atmospheric correction is calculated.

198 Regression fitting of MISR surface reflectance with the newly estimated MISR surface reflectance

199 was performed (60% of the total sample data was randomly selected), and the surface reflectance

200 error correction model was finally established, as shown in the following equation:

201

$$\rho(\theta_s,\theta_v,\phi)_{MISR\_a} = \rho(\theta_s,\theta_v,\phi)_{MODIS\_at} \times \frac{BRDF(\theta_s,\theta_v,\phi)_{MISR}}{BRDF(\theta_s,\theta_v,\phi)_{MODIS}} \qquad (10)$$

202   In Eq. 10, $BRDF(\theta_s,\theta_v,\phi)_{MISR}$ and $BRDF(\theta_s,\theta_v,\phi)_{MODIS}$ are BRDFs obtained under

203 MISR and MODIS angles, respectively. θ_s is the solar zenith angle, θ_v is the satellite zenith

204 angle, and ϕ is the relative azimuth angle. $\rho(\theta_s,\theta_v,\phi)_{MISR\_a}$ is the surface reflectance of

205 MODIS at the geometric observation angle of MISR, and $\rho(\theta_s,\theta_v,\phi)_{MODIS\_at}$ is the MODIS

206 atmospheric corrected reflectance.

207   In this study, spectral data containing the typical characteristics of 28 different types of

208   vegetation, soil and water bodies were selected from 5 standard spectral libraries included with

209   ENVI software. The surface reflectance of MODIS and MISR sensors in the blue band is

210   calculated by the formula (Chen et al., 2021).

211

$$\rho(\theta_s,\theta_v,\phi)_{MISR} = \rho(\theta_s,\theta_v,\phi)_{MISR\_a} \times 0.9834 - 0.0081 \tag{11}$$

212   The New MODIS surface reflectance ($\rho(\theta_s,\theta_v,\phi)_{MISR\_a}$) at the MISR angle obtained from

213   Eq. 10 is converted to the MISR surface reflectance by Eq. 11.

214   The MISR surface reflectance estimated by Eq. 11 was transformed using an error correction

215   model to obtain an improved MISR surface reflectance. The improved MISR surface reflectance

216   will be used for AOD retrieval. The MISR surface reflectance previously estimated based on

217   MODIS V5.2 algorithm was fitted with the MISR surface reflectance estimated based on MODIS

218   atmospheric correction (60% of the data were randomly selected) by linear regression, and a

219   MISR correction model was established, as shown in Eq. 12. The previously estimated 9-angle

220   MISR surface reflectance is corrected by Eq. 12, and the improved surface reflectance of the

221   MISR sensor at 9 angles is obtained, and finally used for MISR AOD retrieval at 9 angles.

222

$$\rho(\theta_s,\theta_v,\phi)_{MISR-b}^{*} = \rho(\theta_s,\theta_v,\phi)_{MISR} \times 0.9209 + 0.0409 \tag{12}$$

223   Where ρ_{MISR-b}^{*} is the improved MISR surface reflectance in Eq. 12.

224   **3.3 Flow of improved multi-angle AOD retrieval**

225   The flow of the improved surface reflectance algorithm in this study is shown in Figure 2.

226   Firstly, the atmospheric correction of MODIS L1B data is performed using 6S model. Then, the

227   MISR surface reflectance estimated by previous study was combined with the new MISR surface

228   reflectance estimated by Eq. 11 to build a MISR error correction model for obtaining the improved

229   MISR surface reflectance (Chen et al., 2021). The study retrieved the MISR AOD for nine camera

230   angles using improved MISR surface reflectance. We validated the improved MISR AOD with

231   AERONET AOD. We compared the improved AOD with the previously retrieved AOD and

232   analyzed the accuracy and spatial distribution trends of the improved AOD. The AOD retrieval

233   method used in this study is based on chen et al. (2021). In our study, we used continental aerosols

234   for AOD retrieval and 6S model for atmospheric correction. Choosing the right aerosol type is

235   crucial for obtaining accurate aerosol optical depth. Previous studies have shown that continental

236   aerosols can be used to estimate aerosol optical depth in the Yangtze River Delta (He et al., 2015).

237   In this study, the same aerosol type was used for AOD retrieval and atmospheric correction, and

238   the error transfer caused by aerosol type and atmospheric correction was not considered.
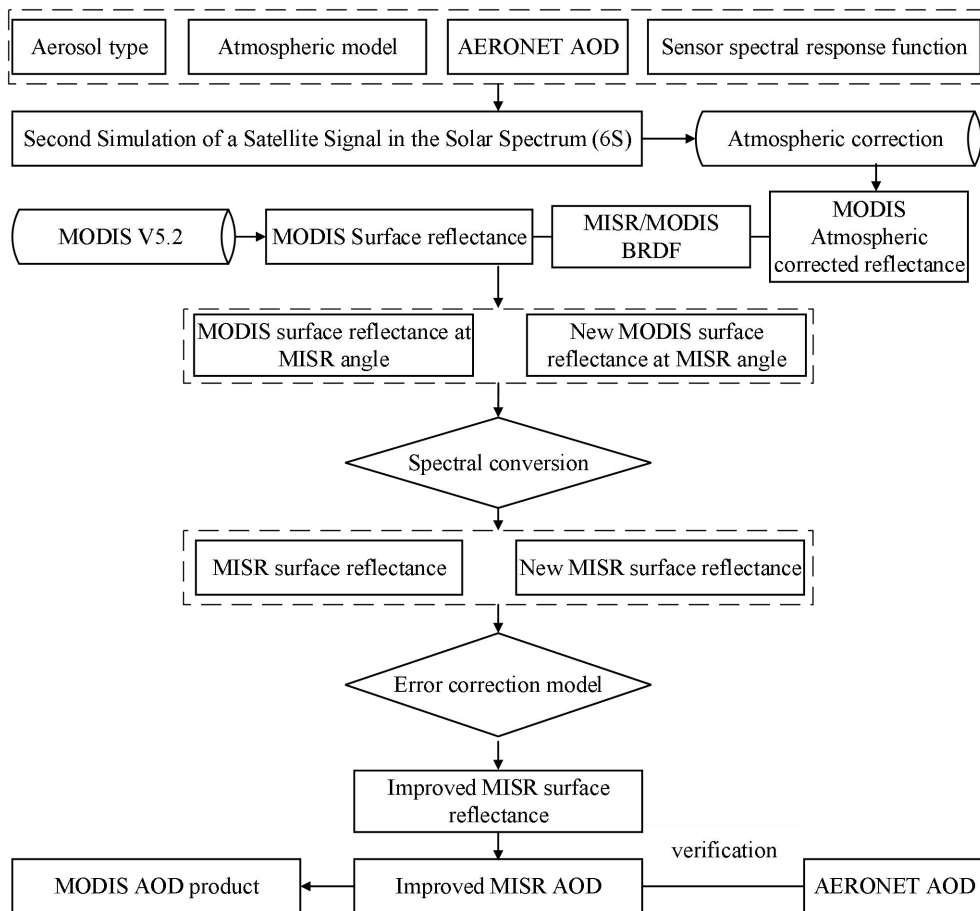
239

240   **Figure 2.** Flow chart of the improved MISR surface reflectance algorithm

4. Results and discussion

4.1 Improved MISR surface reflectance variation characteristics

The variation characteristics of MISR surface reflectance, MISR atmospheric correction reflectance and improved MISR surface reflectance are shown in Figure 3. These values are the average values of all sample data collected at the corresponding locations of the two sites in Taihu and Xuzhou-CUMT during the period of validity from 2016-2018. At Taihu and Xuzhou-CUMT sites, the improved MISR surface reflectance of 9 camera angles is generally higher than that of MISR surface reflectance, and lower than that of MISR atmospheric correction reflectance. The surface reflectance of 9 camera angles MISR is between 0.02 and 0.04. On average, the improved surface reflectance is higher than the previously estimated MISR surface reflectance.
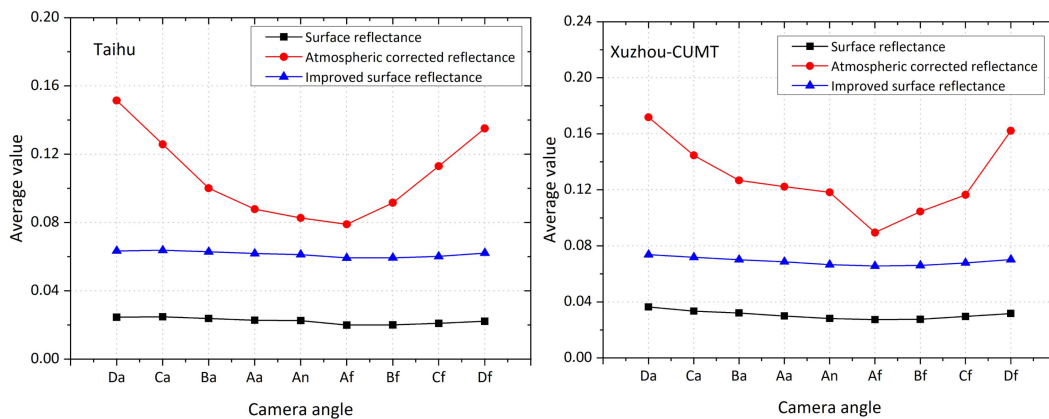
Figure 3. Comparison of MISR surface reflectance, atmospheric corrected reflectance and improved surface reflectance in the blue band (This is multi-year averaged sample data from two sites, Taihu and Xuzhou-CUMT).

To clarify the trend of the improved surface reflectance, the study conducted a time-series analysis of the MISR surface reflectance and the improved surface reflectance. The improved

257   MISR surface reflectance is always higher than the previously estimated MISR surface reflectance

258   (Figure 4). The MISR surface reflectance is generally between 0 and 0.05, while the improved

259   surface reflectance values is about 0.05 to 0.1. Overall, the improved surface reflectance was

260   increased.
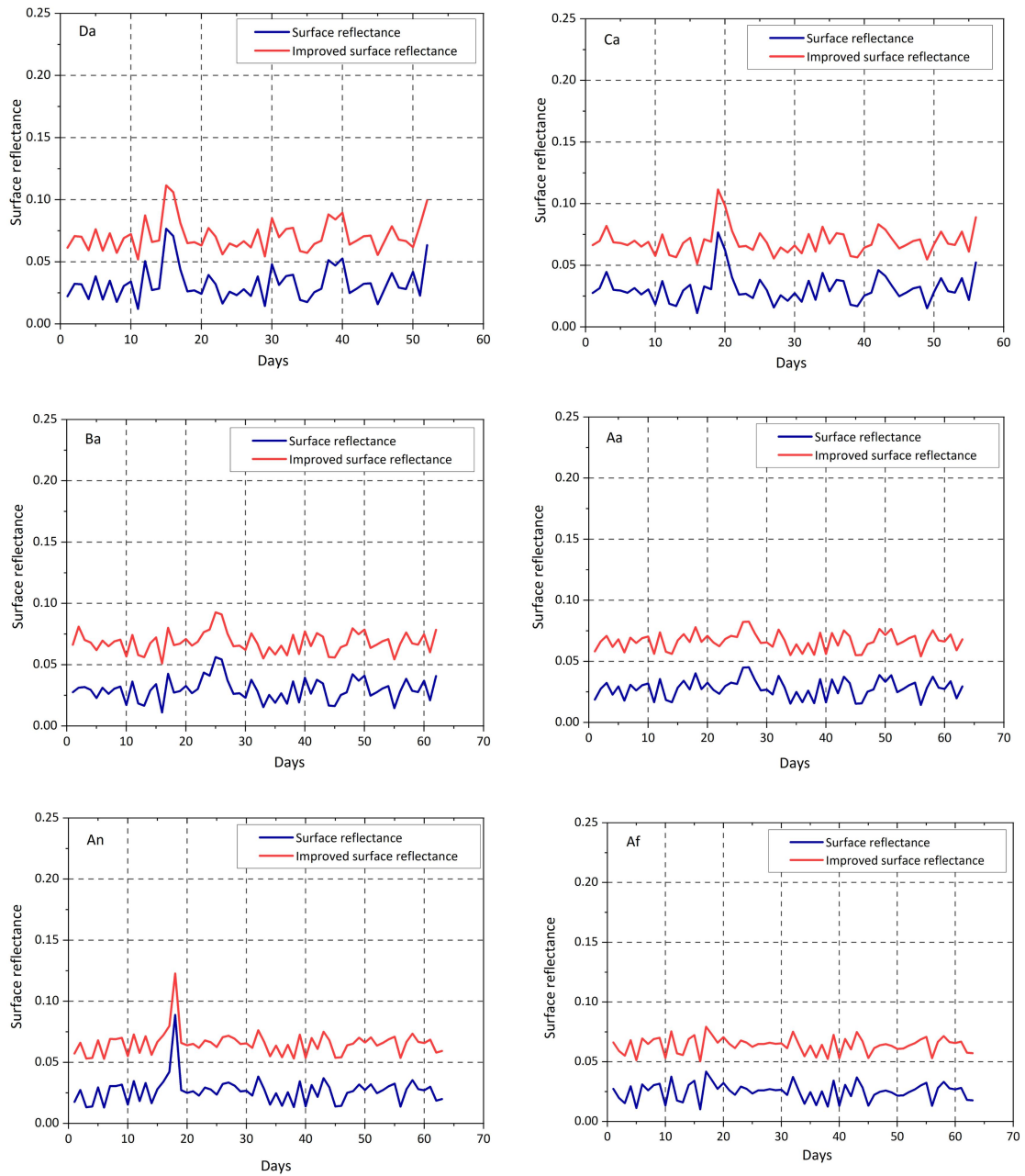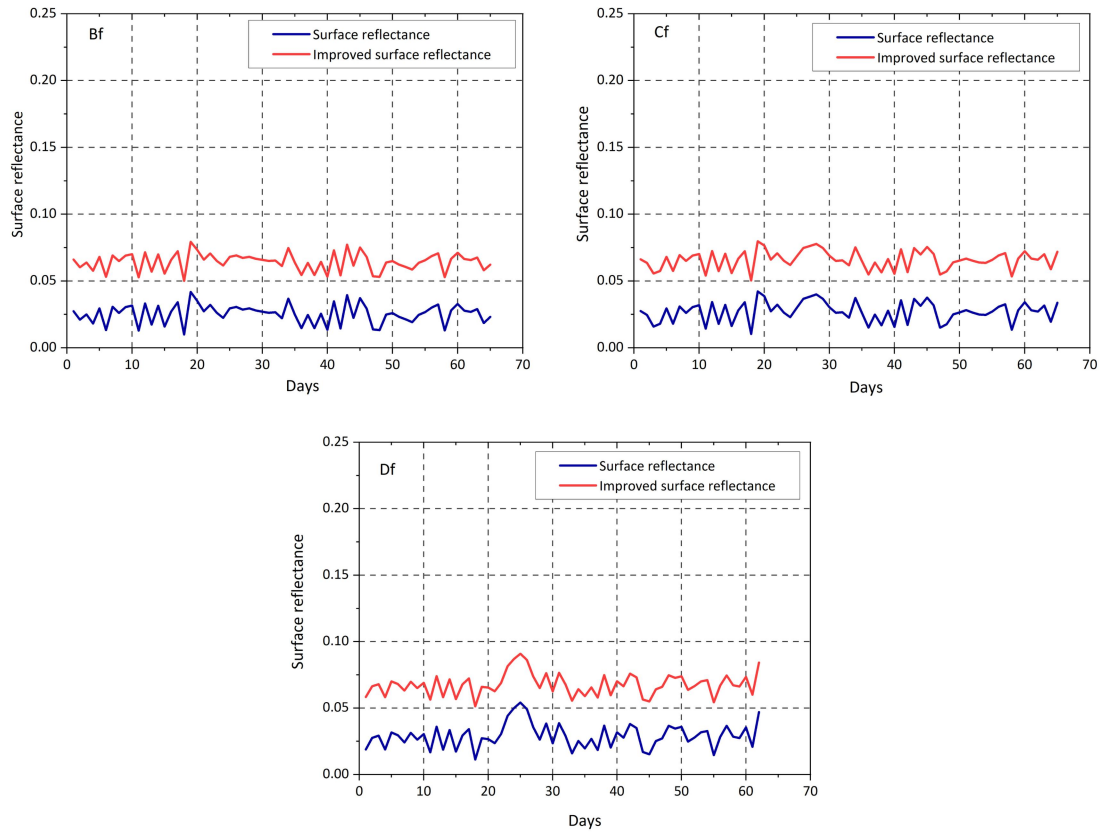
Figure 4. Time series of surface reflectance in the blue band of the MISR sensor for 9 observation

angles (Table S2 lists the time series of the 9 angles from front to back)

4.2 Improved MISR AOD retrieval results

Three years of MISR AOD results were obtained using improved surface reflectance retrieval.

This study gives the results of the retrieval of the MISR sensor on June 12, 2018 for nine camera

observation angles (Figure 5). From the spatial distribution of AOD, it can be seen that the

retrieval results in the study area do not exceed 1. The overall spatial distribution trend is

generally consistent with the pre-improvement results (Chen et al., 2021), but there are differences

in the magnitude of the values. The values in the northeast and south range from 0.5 to 1,

indicating poor air quality in these areas. The AOD values retrieved from 5 camera observation

angles Ba, Aa, An, Af, and Bf are in the approximate range of 0.25-0.5. In the central region, most

272   of the AOD values from the 4 camera observation angles Da, Ca, Cf and Df are in the range of

273   0-0.25. The data show that the air quality in the central region is generally good, and the air

274   pollution level is light in some areas. The higher AOD in southern Shandong and northern Jiangsu

275   may be related to the increased of local aerosol emissions caused by human activities.
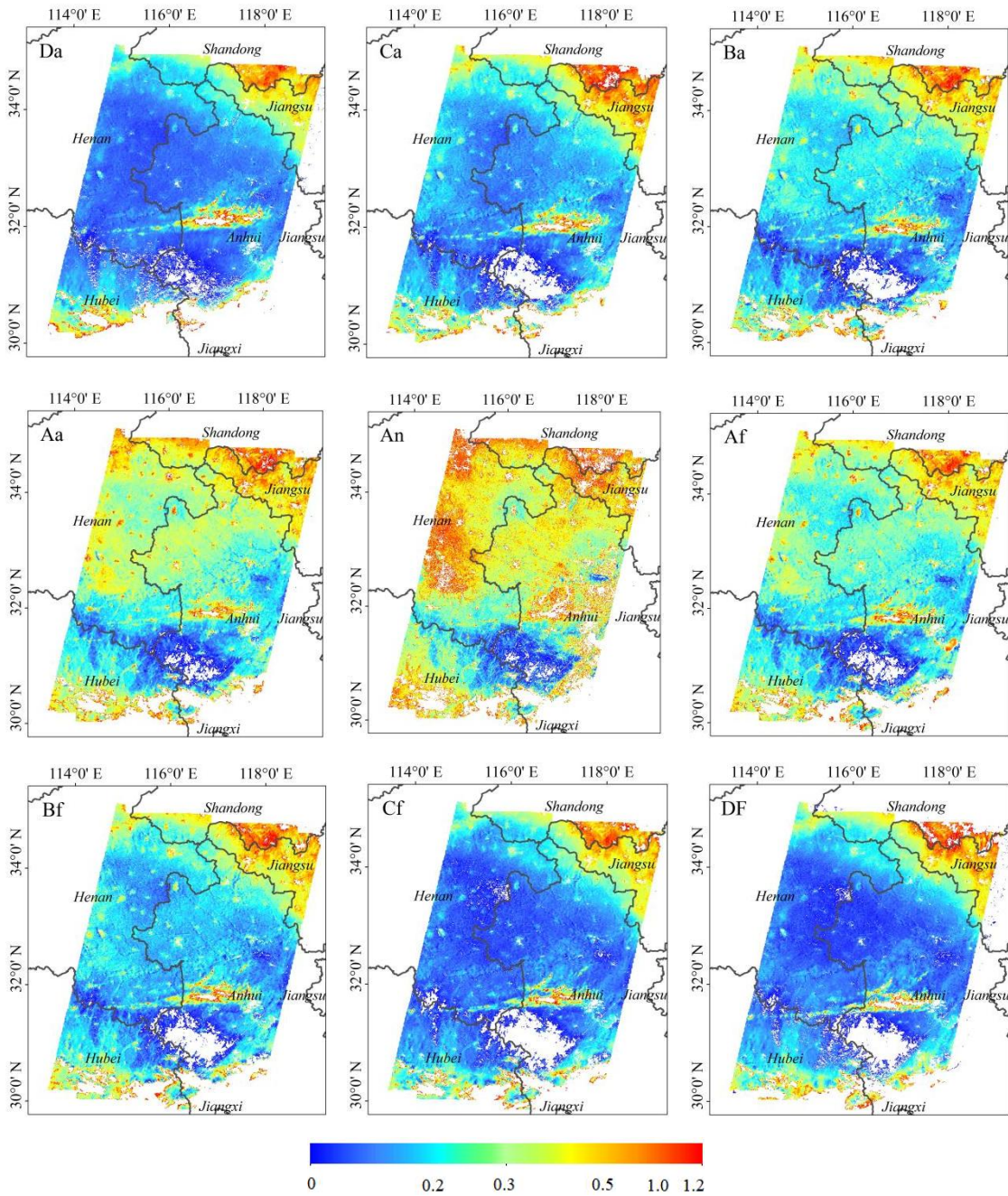
276   **Figure 5.** June 12, 2018 Improved MISR AOD retrieval results at 550 nm

277   The improved MISR AOD spatial distribution results were then validated by comparing them

278   with the MODIS AOD product. The MODIS AOD product has a resolution of 3km. The trends in

279   the spatial distribution of MODIS AOD products are consistent with the improved MISR AOD

280   (Figure 6). However, the MODIS AOD product has more missing data, and the AOD obtained by

281   using the improved algorithm for retrieval can avoid missing data. In addition, the AOD retrieval

282   with the improved algorithm has a higher resolution compared to the image quality of the MISR

283   AOD product.
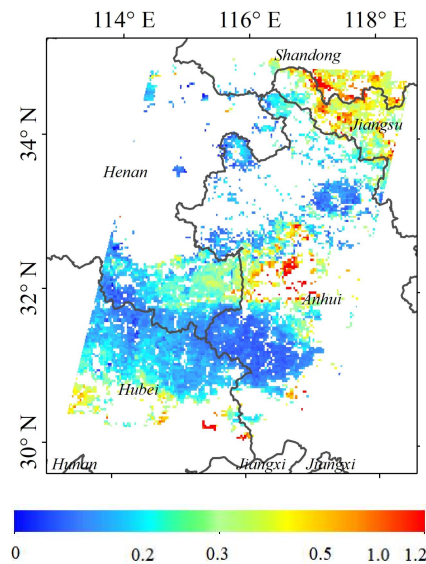
284   **Figure 6.** MODIS AOD 550nm product spatial distribution on June 12, 2018

285   **4.3 Verification of improved MISR AOD**

286   There are many AERONET sites in the Yangtze River Delta region, but currently only two

287   sites, Taihu and Xuzhou-CUMT, are able to provide continuous data, and the other sites acquire

288   data on limited time scales. Therefore, we selected the Taihu and Xuzhou-CUMT sites with more

289   data for verification. To validate the retrieved MISR AODs, we selected valid AOD records in the

290   550nm band within a 30-minute interval between the AERONET ground observation site and the

291   Terra satellite. The MISR sensor 9 camera views take about 7 minutes to be able to observe the

same geographic location at relatively short intervals. Therefore, we used the AERONET AOD

averages as approximate truth values and compared them with the retrieved MISR AODs to

validate and minimize errors due to time lag. Spatially, we selected the image elements observed

by the MISR sensor from nine angles and compared them with the corresponding positional

AERONET observations. Since the sun photometer did not have a wavelength of 550nm

corresponding to the retrieval results, the AOD at 550nm was calculated by applying Angstrom

(Eq. 13).

$$\tau(\lambda) = \beta \lambda^{-\alpha} \tag{13}$$

In the formula, $\tau(\lambda)$ is the AOD at wavelength λ, β is the concentration of aerosols

throughout the atmosphere, and α is the wavelength index of Angstrom.

In this study, four parameters, correlation coefficient (R), root mean square error (RMSE),

p-value and relative mean bias (RMB), will be used to assess the accuracy of the remotely sensed

AOD dataset. The specific calculation principles for the three parameters R, RMSE and RMB are

shown in Eq. 14-16. The validation results of AOD dataset of Taihu and Xuzhou-CUMT sites

during 2016-2018 after improvement in this study are shown in Figure 7 and Figure 8.

Generally, the scatter plots are distributed above and below the 1:1 line. R is a parameter

characterising the correlation between the remote sensing retrieval results and the ground retrieval

results. R reached 0.89 for the Taihu site and 0.85 for the Xuzhou-CUMT site. RMSE is a

parameter characterising the absolute error of the remote sensing retrieval results, and the

minimum RMSE is 0.21 for the Taihu site. The minimum RMSE is 0.20 for the Xuzhou-CUMT

site. RMB is a parameter used to describe the relative error of remote sensing retrieval results, and

the minimum RMB is 0.52 for the Taihu site and 0.32 for the Xuzhou-CUMT site. Overall, the

314   retrieval results at angle An are optimal after algorithm improvements (Taihu: R=0.84, RMB=0.52;

315   Xuzhou-CUMT: R=0.85, RMB=0.47). By comparing the results with the pre-improvement AOD

316   validation, the improved AOD retrieval accuracy has been significantly improved (Table 1). In

317   Table 1, R is the correlation between the AOD retrieval results and AERONET AOD before

318   improvement. RMB is the relative deviation between the AOD retrieval by the pre-improvement

319   algorithm and AERONET AOD. Improved R is the correlation between the improved AOD

320   retrieval results and AERONET AOD. Improved RMB is the relative deviation between the AOD

321   retrieved with the improved algorithm and AERONET AOD.

322
$$R = \frac{\sum_{i=1}^{N}(A_i - \overline{A})(A_i' - \overline{A'})}{\sqrt{\sum_{i=1}^{N}(A_i - \overline{A})^2 \sum_{i=1}^{N}(A_i' - \overline{A'})^2}} \tag{14}$$

323
$$RMSE = \sqrt{\sum_{i=1}^{N}(A_i - A_i')^2 / N} \tag{15}$$

324
$$RMB = \sum_{i=1}^{N}(A_i - A_i') / N \tag{16}$$

325   where A_i is the retrieve MISR AOD, A_i' is the corresponding AERONET AOD, $\overline{A}$

326   and $\overline{A'}$ are the mean values of the retrieve MISR AOD and AERONET AOD, respectively. N is

327   the number of valid matching results for AERONET AOD and MISR AOD.
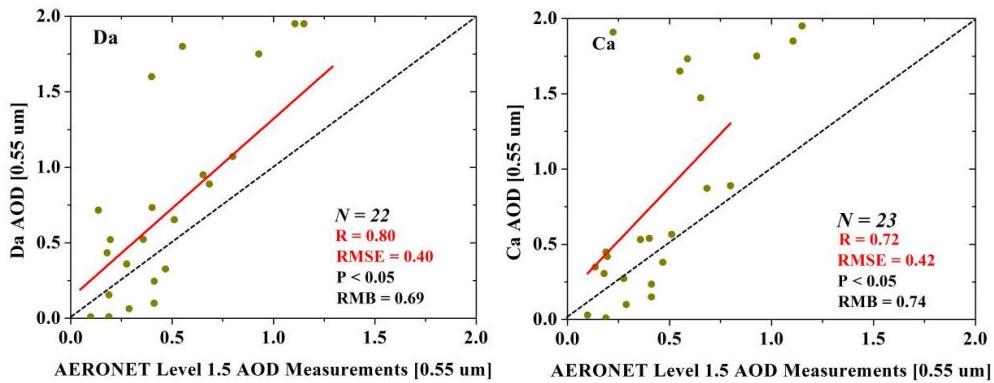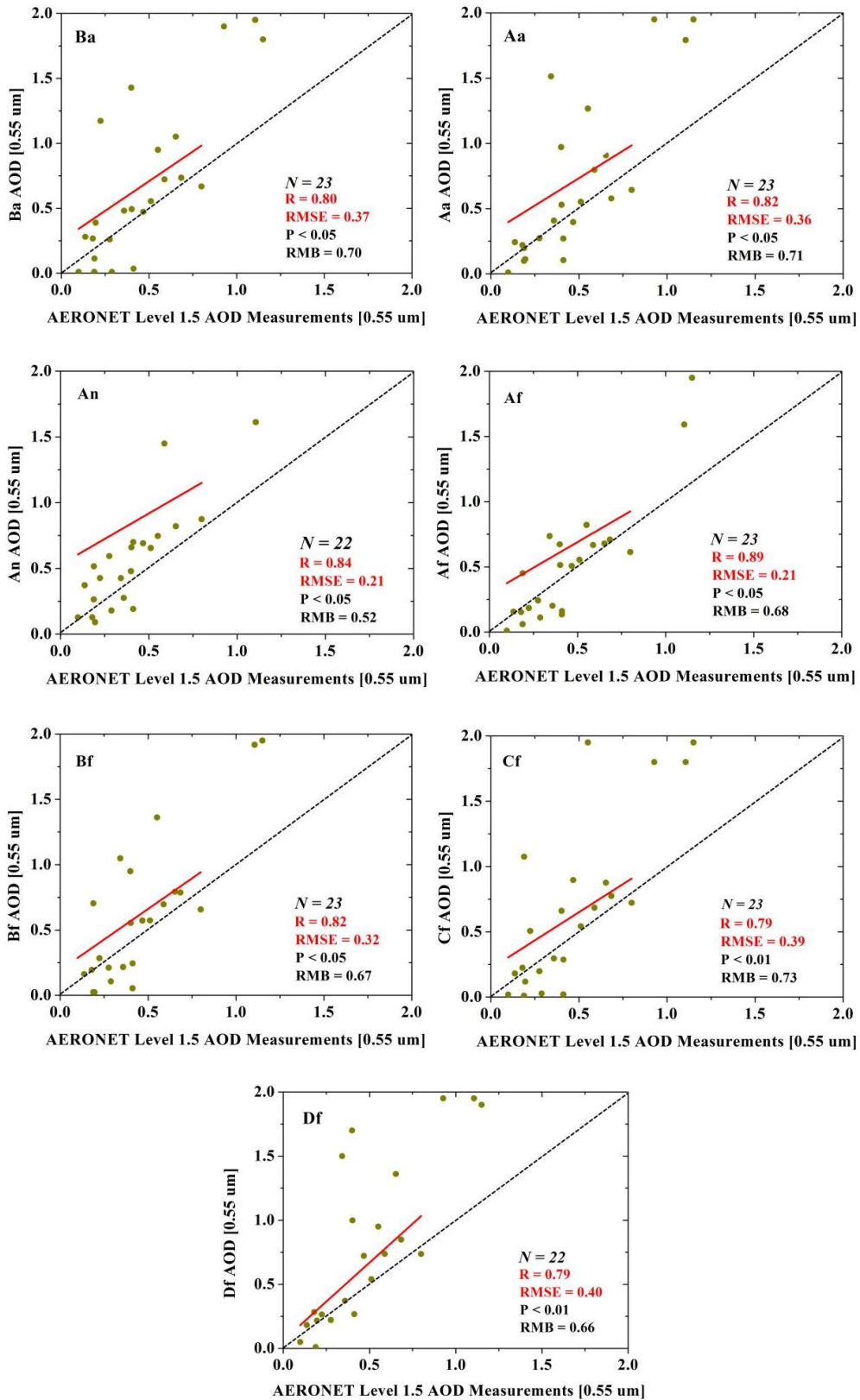
328   **Figure 7.** Comparison between improved MISR AOD and AERONET AOD at Taihu site (N is

329   the number of verification points, red line represents a linear fitting line)
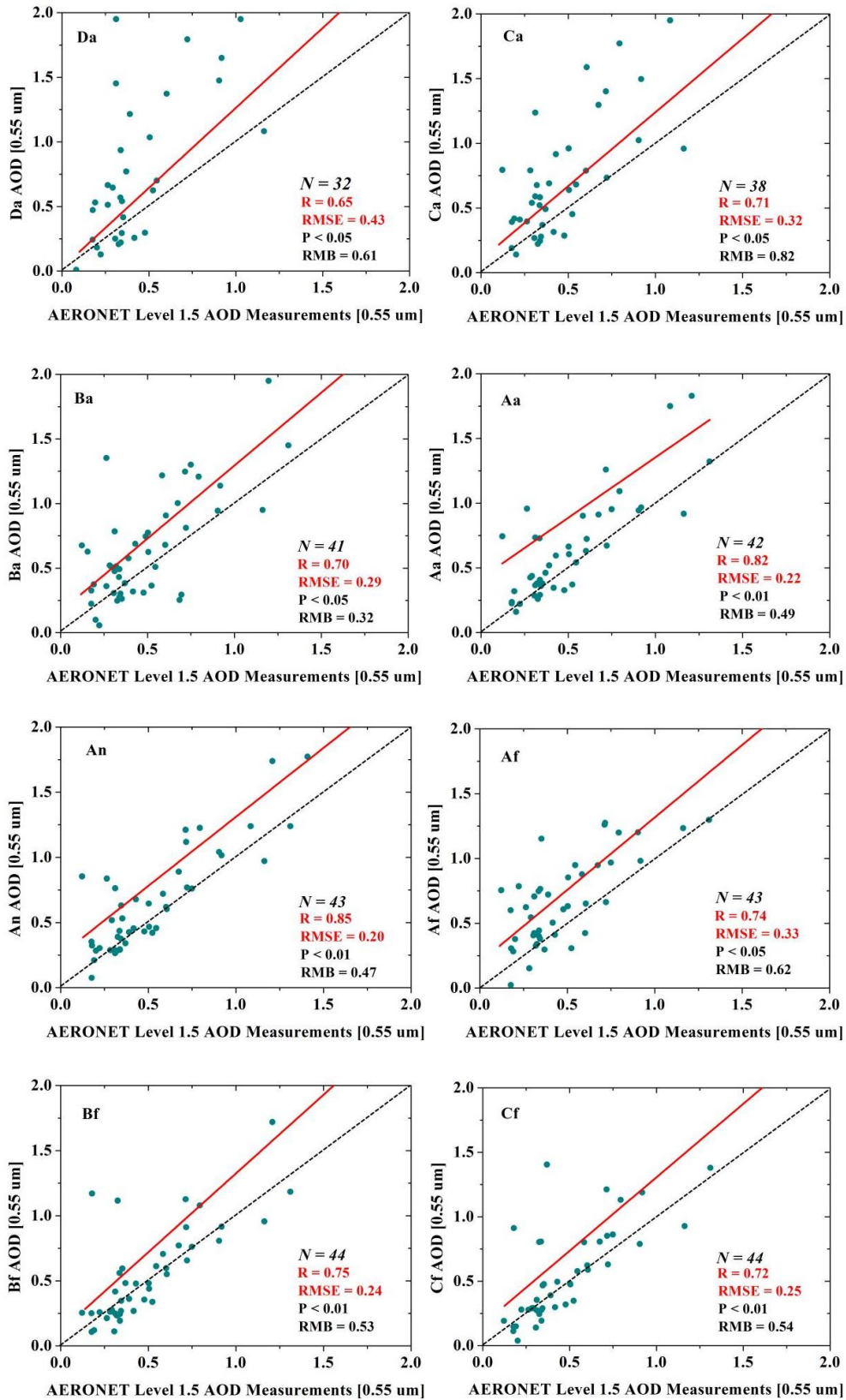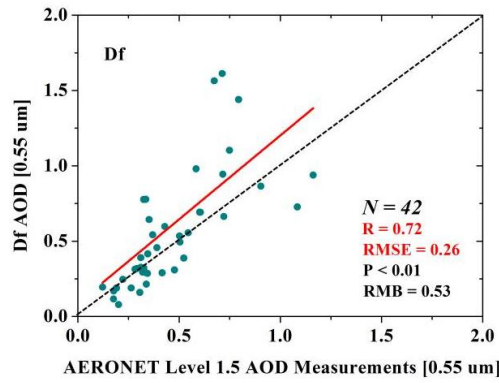
Figure 8. Comparison between improved MISR AOD and AERONET AOD at Xuzhou-CUMT

site (N is the number of verification points, red line represents a linear fitting line)
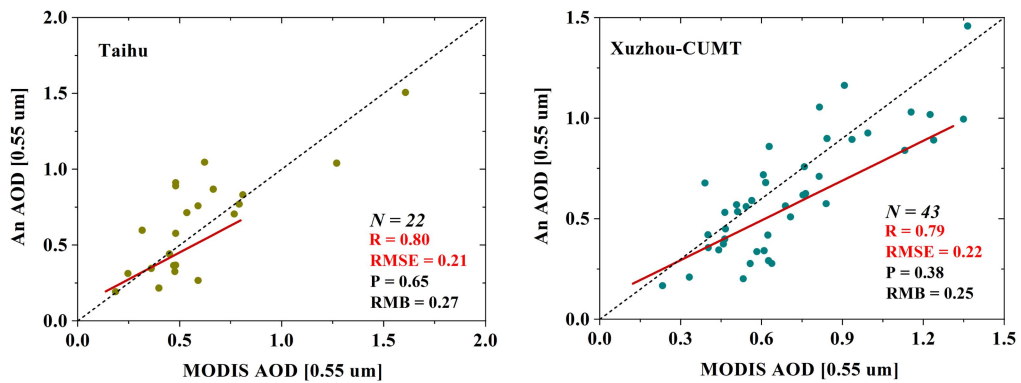
Figure 9. Comparison of validation of retrieved AOD with MODIS AOD product

Table 1. Precision comparison of MISR AOD and AERONET AOD before

and after improvement

Site	Angle	R	RMB	Improved R	Improved RMB
	Da	0.77	1.08	0.80	0.69
	Ca	0.70	1.00	0.72	0.74
	Ba	0.77	0.61	0.80	0.70
	Aa	0.81	0.68	0.82	0.71
Taihu	An	0.45	1.22	0.84	0.52
	Af	0.72	0.87	0.89	0.68
	Bf	0.72	0.60	0.82	0.67
	Cf	0.57	0.65	0.79	0.73
	Df	0.77	0.47	0.79	0.66
Xuzhou-	Da	0.45	1.58	0.65	0.61

CUMT	Ca	0.59	0.96	0.71	0.82
	Ba	0.67	0.78	0.70	0.32
	Aa	0.73	0.78	0.82	0.49
	An	0.75	0.85	0.85	0.47
	Af	0.72	0.63	0.74	0.62
	Bf	0.62	0.65	0.75	0.53
	Cf	0.68	0.66	0.72	0.54
	Df	0.67	0.65	0.72	0.53

336

337 Comparing the validation results of the MODIS AOD product with those of the observation

338 sites (Taihu: R=0.59, RMSE=0.19, P<0.05, RMB=0.52; Xuzhou-CUMT: R=0.71, RMSE=0.25,

339 P<0.05, RMB=0.44) (Chen et al., 2021), we found that the Taihu and Xuzhou-CUMT sites have

340 high correlation between the improved MISR AOD and MODIS AOD products. The smaller

341 observation angle of the improved MISR AOD, the closer the error is to the MODIS AOD product.

342 The observation angle of MISR An is the same as that of MODIS. Therefore, we selected two

343 sites for validation at the An observation angle and MODIS AOD product (Figure 9). The results

344 show that the An AOD retrieval by the improved algorithm correlates well with the MODIS AOD

345 product. The position errors of the two image elements are close to each other. The RMSE of the

346 Xuzhou-CUMT site is slightly higher than that of Taihu site, and the RMB of Taihu site is slightly

347 higher than that of the Xuzhou-CUMT site.

348 **5. Conclusion**

349 In this study, we first explored the problems of estimating surface reflectance in our previous

350 study. We obtained an error correction model for surface reflectance by using a linear fit of the

351 MISR surface reflectance and a new estimate of the MISR surface reflectance. The improved

352 MISR surface reflectance was obtained through the error correction model. We then retrieved a

353   new AOD product using the improved surface reflectance and a lookup table constructed from the

354   6S model. Two AERONET ground observation sites with longer time series were used to validate

355   the AOD obtained by satellites.

356   (1) Overall, the improved AOD and its spatial distribution trends are consistent with our

357   previous results. The AOD estimated by improved method exhibited higher accuracy and a high

358   degree of agreement with the AERONET ground-based observational AOD. Overall, the retrieval

359   results at angle An are optimal after algorithm improvements (Taihu: R=0.84, RMB=0.52;

360   Xuzhou-CUMT: R=0.85, RMB=0.47). The improvements at the Xuzhou-CUMT site are more

361   pronounced compared to the Taihu site.

362   (2) More importantly, the optimal AOD obtained in this study has fewer missing pixels and

363   finer spatial resolution than the MODIS AOD product. Through the validation with MODIS AOD

364   products, the AOD of An optimal angle obtained by the improved algorithm is highly correlated

365   with MODIS AOD products.

366   (3) In future, more aerosol models that conform to the actual situation in the study area can

367   be constructed using the AERONET ground observation data and introduced into the MISR AOD

368   retrieval algorithm to further improve the accuracy of the AOD retrieval results. In this study, the

369   AERONET AOD was used as the true value and as an input for the AOD parameter in the 6S

370   model for atmospheric correction of MISR and MODIS images. We then obtained a surface

371   reflectivity error correction model to retrieve AOD for the entire region. It should be emphasized

372   that the more AERONET sites used to train the corrected model, the more accurate AOD retrieved

373   may be obtained by this method. However, the data from the AERONET ground observation sites

374   were limited. In future, the study area can be expanded on a large scale and for a longer time

375 series.

Acknowledgement

377   This study was supported by the National Natural Science Foundation of China Innovation

378 Research Group Project (42021004), Jiangsu Funding Program for Excellent Postdoctoral Talent

379 (2023ZB482), the Natural Science Foundation of Jiangsu Province of China (BK20220455), and

380 the National Science Foundation of China (42201028).

Competing interests

382   The contact author has declared that none of the authors has any competing interests.

383 **Reference**

384 Berhane, S. A.; Bu, L. Aerosol-Cloud Interaction with Summer Precipitation over Major Cities in

385   Eritrea[J]. Remote Sens-basel, 2021, 13(4):21.

386 Chen, L.; Wang, R.; Han J. Influence of observation angle change on satellite retrieval of aerosol

387   optical depth[J]. Tellus B, 2021, 73.

388 Chen, L.; Fei, Y.; Wang, R. Retrieval of high temporal resolution aerosol optical depth using the

389   GOCI remote sensing data[J]. Remote Sens-basel. 2021, 13:2376.

390 Chen, L.; Wang, R.; Wei, G. A surface reflectance correction model to improve the retrieval of

391   MISR aerosol optical depth supported by MODIS data[J]. Adv Space Res, 2021,

392   67(2):858-867.

393 Dao, Y.; Gong, W. Observed holiday aerosol reduction and temperature cooling over East Asia[J].

394   J Geophys Res-atmos, 2014.

395 Daniel, R.; Steven, S.; Robert, W.; Leo, D. Climate Effects of Aerosol-Cloud Interactions[J].

396   Science, 2014, 343, 379-380.

397 Dehghani, M.; Saeedi, A. A.; Zamanian, Z. A study of the relationship between indoor and outdoor

398   particle concentrations in Hafez hospital in Shiraz[J]. Phys.Rev.C, 2012.

399 Dong, W.; Tao, M.; Xu, X.; Wang, J.; Wang, Y.; Wang, L.; Song, Y.; Fan, M.; Chen, L. Satellite

400   Aerosol Retrieval From Multiangle Polarimetric Measurements: Information Content and

401   Uncertainty Analysis," IEEE Trans. Geosci. Remote Sens. 2023, 61, 1-13.

402 Dubovik, O.; Li.; Mishchenko M. I. Polarimetric remote sensing of atmospheric aerosols:

403   Instruments, methodologies, results, and perspectives[J]. Pergamon, 2019, 474-511.

404 Deuzé, J. L.; Bréon, F. M.; Devaux, C.; Goloub, P.; Herman, M.; Lafrance, B.; Maignan, F.;

405 Marchand, A.; Nadal, F.; Perry, G.; Tanré, D. Remote sensing of aerosols over land surfaces

406 from POLDER-ADEOS-1 polarized measurements. J Geophys Res-atmos, 2001, 106(D5):

407 4913-4926.

408 Giles, D. M.; Sinyuk, A.; Sorokin, M. G. Advancements in the Aerosol Robotic Network

409 (AERONET) Version 3 database-automated near-real-time quality control algorithm with

410 improved cloud screening for Sun photometer aerosol optical depth (AOD) measurements[J].

411 Copernicus GmbH, 2019, 12(1), 169-209.

412 Gupta, P.; Levy, R. C.; Mattoo, S. A surface reflectance scheme for retrieving aerosol optical depth

413 over urban surfaces in MODIS dark target retrieval algorithm[J]. Atmos Meas Tech, 2016,

414 9(7): 3293-3308.

415 Hatzianastassiou, N. The direct effect of aerosols on the radiation budget and climate of the

416 Earth-atmosphere system: its variability in space and time. EGU General Assembly

417 Conference Abstracts EGU General Assembly Conference Abstracts, 2009.

418 Holben, B. N.; Tanré, D.; Smirnov, A. An emerging ground-based aerosol climatology: Aerosol

419 optical depth from AERONET[J]. J Geophys Res, 2001, 106, 12067-12097.

420 Huang, X.; Ding, A. Aerosol as a critical factor causing forecast biases of air temperature in global

421 numerical weather prediction models[J]. Science Bulletin, 2021.

422 Hsu, N. C.; Tsay, S. C.; King, M. D. Aerosol properties over bright-reflecting source regions[J].

423 IEEE Trans. Geosci. Remote Sens, 2004, 42(3):557- 569.

424 Kaufman, Yoram J. The MODIS 2.1-um channel--correlation with visible reflectance for use in

425 remote sensing of aerosol.[J]. IEEE T Geosci Remote, 1997, 35, 1286-1298.

426 Kokhanovsky, A. A.; Curier, R. L.; Leeuw, G. D.; Grey, W. M. F. The intercomparison of AATSR

427   dual-view aerosol optical thickness retrievals with results from various algorithms and

428   instruments. Int. J. Remote Sens. 2009, 30 (17): 4525-4537.

429   Lee, S. S.; Donner L. J.; Penner J. E. Thunderstorm and stratocumulus: How does their contrasting

430   morphology affect their interactions with aerosols?[J]. Atmos. Chem. Phys. 2010, 10(2),

431   6819-6837.

432   Li, E.; Zhang, Z.; Tan, Y. A Novel Cloud Detection Algorithm Based on Simplified Radiative

433   Transfer Model for Aerosol Retrievals: Preliminary Result on Himawari-8 Over Eastern

434   China[J]. IEEE T Geosci Remote, 2020, 59(3):1-12.

435   Li, Y.; Xue, Y.; Guang, J. Ground-Level PM2.5 Concentration Estimation from Satellite Data in

436   the Beijing Area Using a Specific Particle Swarm Extinction Mass Conversion Algorithm[J].

437   Remote Sens-basel, 2018, 10(12), 1906.

438   Lu, S.; Xue, Y.; Yang, X.-H.; Leys, J.; Guang, J.; Che, Y.-H.; Fan, C.; Xie, Y.Q.; Li, Y. Joint

439   Retrieval of Aerosol Optical Depth and Surface Reflflectance Over Land Using

440   Geostationary Satellite Data. IEEE Trans. Geosci. Remote Sens. 2019, 57, 1489–1501.

441 Mironova, I. A. Aerosols over continental Portugal (1978-1993): their sources and an impact on

442   the regional climate[J]. Atmos. Chem. Phys. 2015, 15(11):6407-6418.

443 Remer, L. A; Tanré, D.; Kaufman, Y. J. Algorithm for remote sensing of tropospheric aerosol from

444   MODIS: Collection 005[J]. 2009.

445 Samset, B. H.; Sand, M.; Smith, C. J. Climate Impacts From a Removal of Anthropogenic Aerosol

446   Emissions[J]. Geophys Res Lett, 2018, 45(2).

447 Sun, E.; Fu, C.; Yu, W. Variation and Driving Factor of Aerosol Optical Depth over the South

448   China Sea from 1980 to 2020[J]. Atmosphere, 2022, 13, 372.

449   Sundstrom, A. M.; Kolmonen, P.; Sogacheva, L.; Leeuw, G. D. Aerosol retrieval over China with

450   the AATSR dual view algorithm. Remote Sens. Environ. 2012, 116 (1): 189-198.

451   Xie, Y.; Xue, Y.; Jie, G. Deriving a Global and Hourly Data Set of Aerosol Optical Depth Over

452   Land Using Data From Four Geostationary Satellites: GOES-16, MSG-1, MSG-4, and

453   Himawari-8[J].IEEE T Geosci Remote, 2019, 99:1-12.

454   Zhang, Y.; Li, Z.; Liu, Z. Retrieval of aerosol fine-mode fraction over China from satellite

455   multiangle polarized observations: validation and comparison[J]. Atmos Meas Tech, 2021, 2,

456   1655-1672.